The NOAA Microwave Integrated Retrieval System (MiRS): Validation of Precipitation From Multiple Polar-Orbiting Satellites

Shuyan Liu, Christopher Grassotti, Quanhua Liu, Yong-Keun Lee, Ryan Honeyager, Yan Zhou, and Ming Fang

***Abstract*—This article describes a multisatellite validation study of precipitation from the microwave integrated retrieval system (MiRS). MiRS is a variational algorithm designed to process passive microwave measurements using a common core of retrieval software, and currently runs operationally on data from ten different earth-observing satellites. The primary validation was conducted for the polar-orbiting satellites SNPP, NOAA20 (both bearing the ATMS instrument), MetopB, and MetopC (both bearing the AMSUA and MHS instruments) during the period from December 1, 2018 through December 31, 2019. Validation was conducted using operational ground-based radar-rain gauge analyses from Stage-IV and multiradar multisensor (MRMS) over the continental United States. Results indicate that the precipitation estimates are largely consistent with one another and that agreement with ground-based analyses has a strong seasonal component. Warm season performance is generally higher and more stable than during the cold season. SNPP and NOAA20 estimates appeared to show slightly higher biases, outside of July and August. Frequency distributions of precipitation intensity also showed better agreement between MiRS and Stage-IV for higher precipitation rates in the warm season, highlighting the difficulty of estimating over land precipitation rates associated with stratiform precipitation systems that typically occur during the cold season. All satellites depicted the annual mean precipitation rate global distribution with good interconsistency, but with some differences possibly related to individual temporal sampling characteristics of each satellite. Summary validation statistics and scores stratified by season show that MiRS performance metrics using MRMS as a reference are largely similar to those based on using Stage-IV.**

***Index Terms*—Advanced microwave sounding unit-A (AMUSA)-microwave humidity sounder (MHS), advanced technology microwave sounder (ATMS), microwave integrated retrieval system (MiRS), precipitation rate, satellite.**

I. Introduction

ACCURATE precipitation rate retrieval around the globe is crucial for applications such as extreme weather event detection, flood and drought monitoring, and climate change monitoring. Retrieval techniques based on space-based measurements began in the 1970s with the widespread deployment of meteorological satellites equipped with visible, infrared, and microwave instruments [1]. The advantages of global coverage compared to ground-based measurements such as radar and rain gauges have led to the development of many precipitation algorithms that process satellite radiances.

Because microwave radiances are more directly related to the quantity of liquid and frozen hydrometors in the atmospheric column by sensing the emission and scattering of the particles, these measurements can thus be used to provide physically reasonable retrievals of precipitation rate. Many precipitation algorithms using microwave radiances were developed based on special sensor microwave imager (SSM/I) onboard Defense Meteorological Satellite Program (DMSP) since the first SSM/I was providing well calibrated data since 1987 [2]–[9]. Wilheit *et al.* [10] overviewed 16 precipitation retrieval algorithms that use SSM/I high-frequency scattering measurement, low-frequency emission measurements, and combinations. Petty [11] developed a physical inversion-based algorithm which used three channels from low and high frequencies plus a scattering index derived from high-frequency channel measurements to retrieve the precipitation rate over the ocean. After the Tropical Rainfall Measuring Mission (TRMM) was launched in 1997, precipitation algorithms were further developed [12], [13] since the microwave imager (TMI) had additional low-frequency

Manuscript received February 26, 2020; revised May 8, 2020 and May 28, 2020; accepted June 1, 2020. Date of publication June 5, 2020; date of current version June 18, 2020. This work was supported in part by the National Oceanic and Atmospheric Administration Joint Polar Satellite System Program Office under Grant NA19OAR4320073 at the Cooperative Institute for Research in the Atmosphere, in part by Colorado State University, and in part by the University of Maryland/Earth System Science Interdisciplinary Center (ESSIC) under Grant NA14NES4320003 at the Cooperative Institute for Climate and Satellites (CICS). *(Corresponding author: Shuyan Liu.)*

Shuyan Liu is with the Cooperative Institute for Research in the Atmosphere, Colorado State University, Fort Collins, CO 80523 USA (e-mail: shuyan.liu@noaa.gov).

Christopher Grassotti and Yong-Keun Lee are with the Cooperative Institute for Satellite and Earth System Studies, Earth System Science Interdisciplinary Center, University of Maryland, College Park, MD 20740 USA, and also with the National Oceanic and Atmospheric Administration Center for Satellite Applications and Research, National Environmental Satellite, Data, and Information Service, College Park, MD 20740 USA (e-mail: christopher.grassotti@noaa.gov; yong-keun.lee@noaa.gov).

Quanhua Liu is with the National Oceanic and Atmospheric Administration Center for Satellite Applications and Research, National Environmental Satellite, Data, and Information Service, College Park, MD 20740 USA (e-mail: quanhua.liu@noaa.gov).

Ryan Honeyager is with the Environmental Modeling Center, National Oceanic and Atmospheric Administration National Centers for Environmental Prediction, University Corporation for Atmospheric Research, College Park, MD 20740 USA (e-mail: ryan.honeyager@noaa.gov).

Yan Zhou is with the Cooperative Institute for Satellite and Earth System Studies, Earth System Science Interdisciplinary Center, University of Maryland, College Park, MD 20740 USA (e-mail: yanzhou@umd.edu).

Ming Fang is with the I.M. Systems Group, College Park, MD 20740 USA, and also with the National Oceanic and Atmospheric Administration Center for Satellite Applications and Research, National Environmental Satellite, Data, and Information Service, College Park, MD 20740 USA (e-mail: ming.fang@noaa.gov).

Digital Object Identifier 10.1109/JSTARS.2020.3000348

channels that provided more emission information and at a higher spatial resolution compared with previous microwave instruments. The Goddard profiling algorithm (GPROF) developed by Kummerow *et al.* [13] uses a Bayesian inversion for all surface types. The algorithm then evolved to a fully parametric approach [14] and is applied to data from the Global Precipitation Mission (GPM) microwave imager (GMI) which launched in 2014. Both TRMM and GPM carry spaceborne radars which represent a significant advancement in the ability to more directly detect and measure vertical profiles of liquid and frozen hydrometeors.

The microwave integrated retrieval system (MiRS),[1] is a retrieval algorithm that uses the same core software when applied to any of its supported satellites. MiRS is an inversion algorithm based on physical forward modeling and can invert observed multichannel radiances simultaneously to determine key components of the atmosphere and surface states, including precipitation parameters [15]–[18]. MiRS has been routinely producing satellite-based retrieval products since 2007 at the National Oceanic and Atmospheric Administration (NOAA). Iturbide-Sanchez *et al.* [19] assessed MiRS precipitation retrievals based on six satellites and indicated that the algorithm has comparable skills with other precipitation estimation techniques. Liu *et al.* [20] evaluated MiRS products based on GPM/GMI and compared precipitation with ground-based observation.

MiRS precipitation products from various satellites have been used as input to other multisensor precipitation rate analyses/products such as Climate Prediction Center MORPHing technique (CMORPH) [21], [22], and the National Environmental Satellite, Data, and Information Service (NESDIS) operational blended rain rate product.

The two recently launched polar-orbiting satellites of MetopC and NOAA20 are the follow-on missions to MetopB and SNPP, respectively. Together, they provide timely, critical information with global coverage that help to monitor meteorological events. This article focuses on MiRS precipitation rate retrievals from microwave sensors onboard four satellites: ATMS (advanced technology microwave sounder) onboard NOAA20 and the Suomi National Polar-orbiting Partnership satellite (SNPP), AMSUA (advanced microwave sounding unit-A)-MHS (microwave humidity sounder) onboard MetopC and MetopB. The rest of this article is organizes as follows. Section II introduces the MiRS algorithm and describes the four satellites and microwave instruments. Section III includes results and discussion and finally, Section IV concludes this article.

II. Algorithm, Data, and Evaluation Method

A. MiRS Algorithm and Precipitation Rate Estimation

MiRS is an iterative, physical-based 1-D variational (1-DVAR) retrieval algorithm [23], [24] which solves simultaneously for surface (i.e., emissivity and skin temperature) and atmospheric (i.e., temperature, water vapor, and hydrometeors) parameters. The objective is to minimize a two-term penalty function, which is composed of the departure of the simulated radiances from the observed satellite radiances and the departure of the retrieved parameters from their respective *a priori* backgrounds. The penalty for the simulated radiances departing from measurements is weighted by instrument and radiative transfer modeling error, and the penalty for the retrieved parameters departing from background is weighted by the background error covariance matrix.

MiRS uses the community radiative transfer model (CRTM) [25], [26] as the forward and adjoint operator to simulate radiances and generate the corresponding Jacobians (derivatives) under clear, cloudy, and rainy conditions. The Jacobian matrix contains the sensitivity of radiances to the changes in parameters to retrieve. CRTM has been validated against various satellite measurements [27], [28]. The model is able to simulate multiple scattering effects due to ice, rain, snow, graupel, and cloud at all microwave frequencies and is able to generate the corresponding Jacobians for all atmospheric and surface parameters.

Within the retrieval iterative loop, the 1-DVAR optimal estimation normally uses the *a priori* mean values as a first guess of the state vector. The cost function is calculated for each iteration step. Convergence is achieved if the sum of squared residuals (observed minus simulated radiances normalized by each channel's corresponding combined instrument and forward model noise) is less than one. In practice, MiRS global convergence rates approach 95%. Further details of the MiRS algorithm and iterative approach can be found in Liu *et al.* [20] and Boukabara *et al.* [18], for example.

Precipitation rate is calculated by a postprocessing algorithm that takes advantage of the physical relationship found between atmospheric hydrometeor amounts and surface precipitation rate. Previous work has reported the use of a relationship between IWP and surface precipitation rate to derive surface precipitation fields over ocean and land surfaces [9], [15]. The 1-DVAR in MiRS retrieves rain water content and graupel water content on 100 pressure layers. These hydrometeor profiles are vertically integrated to obtain cloud liquid water (CLW), rain water path (RWP), and graupel water path (GWP); then, precipitation rate is calculated by the following empirical relationship:

$$\mathrm{PR}_{\mathrm{clw}} = C_1 \times (\mathrm{CLW})^{C_2}$$

$$\mathrm{PR} = \mathrm{PR}_{\mathrm{clw}} + C_3 \times (\mathrm{RWP} + \mathrm{GWP})^{C_4}$$

where PR represents the precipitation rate given in millimeters per hour, and $C_1 = 2.339$, $C_2 = 1.156$, $C_3 = 3.897$, and $C_4 = 1.103$ are predefined regression coefficients.

Precipitation rate is only computed within MiRS if the RWP and GWP are greater than 0.005 mm and CLW is greater than 0.275 mm. The CLW threshold is also used to determine the presence of precipitation. The CLW retrieved in MiRS was assessed by Liu *et al.* [29] and the thresholds are in agreement with the values reported in [30]. Precipitation is retrieved over all land and ocean areas not classified as ice or snow covered. The version of MiRS used in this study is v11.4, which is the current operational version as of 2019.

B. Satellites and Sensors

MetopC was launched into a morning overpass orbit of ~9:30 A.M. on November 7, 2018 and is the third and final

[1][Online] Available: https://www.star.nesdis.noaa.gov/mirs/

TABLE I
ATMS CHANNEL INFORMATION

Chan. No.	Central Freq. (GHz) (Polarization)	Band Width (MHz)	NEDT[a] (K)	Beam Width (deg)	FOV[b] size (nadir) (km)
1	23.8 (V)	270	0.9	5.2	74.8
2	31.4 (V)	180	0.9	5.2	74.8
3	50.3 (H)	180	1.2	2.2	31.6
4	51.76 (H)	400	0.75	2.2	31.6
5	52.8 (H)	400	0.75	2.2	31.6
6	53.596±0.115 (H)	170	0.75	2.2	31.6
7	54.4 (H)	400	0.75	2.2	31.6
8	54.94 (H)	400	0.75	2.2	31.6
9	55.5 (H)	330	0.75	2.2	31.6
10	57.290344 (H)	330	0.75	2.2	31.6
11	57.290344±0.217 (H)	78	1.2	2.2	31.6
12	57.290344±0.322±0.048 (H)	36	1.2	2.2	31.6
13	57.290344±0.322±0.022 (H)	16	1.5	2.2	31.6
14	57.290344±0.322±0.010 (H)	8	2.4	2.2	31.6
15	57.290344±0.322±0.0045 (H)	3	3.6	2.2	31.6
16	88.2 (V)	2000	0.5	2.2	31.6
17	165.5 (H)	3000	0.6	1.1	15.8
18	183.31±7.0 (H)	2000	0.8	1.1	15.8
19	183.31±4.5 (H)	2000	0.8	1.1	15.8
20	183.31±3.0 (H)	1000	0.8	1.1	15.8
21	183.31±1.8 (H)	1000	0.8	1.1	15.8
22	183.31±1.0 (H)	500	0.9	1.1	15.8

[a]NEDT: Noise equivalent differential temperature.
[b]FOV: Field-of-view.

TABLE II
AMSUA-MHS CHANNEL INFORMATION

Chan. No.	Central Freq. (GHz) (Polarization)	Band Width (MHz)	NEDT[a] (K)	Beam Width (deg)	FOV[b] size (nadir) (km)
AMSUA					
1	23.8 (V)	270	0.3	3.3	48
2	31.4 (V)	180	0.3	3.3	48
3	50.3 (V)	180	0.4	3.3	48
4	52.8 (V)	400	0.25	3.3	48
5	53.596±0.115 (H)	170	0.25	3.3	48
6	54.4 (H)	400	0.25	3.3	48
7	54.94 (V)	400	0.25	3.3	48
8	55.5 (H)	330	0.25	3.3	48
9	57.29 (H)	330	0.25	3.3	48
10	57.29±0.217 (H)	78	0.4	3.3	48
11	57.29±0.322±0.048 (H)	36	0.4	3.3	48
12	57.29±0.322±0.022 (H)	16	0.6	3.3	48
13	57.29±0.322±0.01 (H)	8	0.8	3.3	48
14	57.29±0.322±0.0045 (H)	3	1.2	3.3	48
15	89.0 (V)	< 6000	0.5	3.3	48
MHS					
16	89.0 (V)	2800	0.22	1.11	16
17	157.0 (V)	2800	0.34	1.11	16
18	183.31±1.0 (H)	2×500	0.51	1.11	16
19	183.31±3.0 (H)	2×1000	0.40	1.11	16
20	190.31 (V)	2200	0.46	1.11	16

[a]NEDT: Noise equivalent differential temperature.
[b]FOV: Field-of-view.

satellite in its series. It was preceded by MetopB which was launched on September 17, 2012, also into a morning orbit. Both satellites contain AMSUA and MHS with combined 20 channels, which provide input to the MiRS algorithm. The data from the instruments on Metop complement the observations collected by NOAA's afternoon orbit satellites of the Joint Polar Satellite System (JPSS). Table I lists AMSUA and MHS channel information, including central frequency, polarization, bandwidth, noise equivalent differential temperature (NEDT), beam width, and ground footprint size at nadir.

NOAA20 is the second of NOAA's JPSS series of polar-orbiting satellites. The satellite was launched on November 18, 2017 and joined SNPP in the same ∼1:30 P.M. afternoon overpass orbit. The SNPP was launched on October 18, 2011. NOAA20 operates about 50 min ahead of SNPP, allowing important overlap in observational coverage. Both of the satellites include ATMS with 22 channels operating in cross-track scanning mode. The ATMS sensor information is listed in Table II.

Both ATMS and AMSUA-MHS contain channels whose frequencies are selected to provide information on atmospheric temperature, water vapor, clouds, hydrometeors, as well as surface conditions. The satellites chosen for the study represent the four most recently launched polar-orbiting operational satellites with passive microwave instruments from both the United States (NOAA) and Europe (EUMETSAT).

C. Validation Dataset and Evaluation Method

To evaluate MiRS precipitation rate retrievals over the continental United States (CONUS), we used Stage-IV radar-gauge composites [20], [31]. Stage-IV is a 4-km gridded precipitation analysis over CONUS produced by the National Centers for Environmental Prediction (NCEP). The data are based on the multisensor precipitation estimator (MPE) analyses known as Stage-III, which use multisensor data (WSR-88D radar and gauges) and are specified on 4-km polar-stereographic grids produced by the 12 River Forecast Centers. In this article, we used the hourly products that are collocated with ATMS and AMUSA-MHS footprints for validation. The collocation process, which matched the gridded Stage-IV analyses to the satellite estimates, accounted for the change in FOV size with satellite viewing angle. This article evaluates precipitation rate performance over land only as the reference dataset has limited coverage and large uncertainty over ocean.

Performance of the retrieval system was evaluated both objectively by statistical and categorical scores. Subjective evaluation

TABLE III
PENTAD PRECIPITATION RATE TIME SERIES CORRELATION COEFFICIENTS DURING DECEMBER 1, 2018–DECEMBER 30, 2019

	Stage-IV	MRMS
MetopB	0.83	0.86
MetopC	0.85	0.87
NOAA20	0.86	0.86
SNPP	0.90	0.89

was done by viewing the spatial distribution for many precipitation events, of which one is presented here. Histograms of precipitation frequency distributions were also compared. Statistical evaluations include comparison of bias, standard deviation, correlation coefficient, and three categorical scores [32], i.e., probability of detection (POD), false alarm ratio (FAR), and Heidke skill score (HSS). POD, also called hit rate, represents an occurrence of a precipitation retrieval greater than the threshold value when Stage-IV observed precipitation rate also exceeds the threshold value and is defined by POD = (number of precipitation event correctly retrieved by MiRS)/(total number of Stage-IV observed precipitation events). FAR, the fraction of the retrieval of precipitation associated with nonoccurrences, represents an occurrence of precipitation retrieval greater than the threshold value when Stage-IV observed precipitation rate did not exceed the threshold value and is calculated by FAR = (false alarms)/(number of MiRS precipitation retrievals). HSS measures the fraction of correct precipitation retrievals after eliminating those retrievals which would be correct purely due to random chance. Thus, HSS = (correct retrieval proportion–proportion correct by chance)/(perfect score–proportion correct by chance), in which a perfect score = 1.

Comparisons were also made for the same time period and in the same manner using the operational multiradar multisensor (MRMS) product as a reference [33]. The MRMS precipitation is derived using WSR-88 Doppler radar data, gauge data, and rapid update cycle (RAP) model hourly analysis fields as input through a quantitative precipitation estimation (QPE) algorithm. The MRMS dataset used in this article is hourly gauge-adjusted precipitation product with 0.01° spatial resolution and collocated with MiRS at satellites footprint. For the sake of brevity, we present only a summary intercomparison of the Stage-IV versus MRMS validation results, with the main conclusion being that retrieval performance against both references is largely the same (see Tables IV and V).

TABLE IV
PERFORMANCE METRICS FOR PRECIPITATION RATE RETRIEVALS VALIDATED BY STAGE-IV

	Bias (mm/hr)	Stdv (mm/hr)	Corr	POD	FAR	HSS
Winter (December 1, 2018 – February 28, 2019)						
MetopB	-0.013	0.57	0.56	0.55	0.042	0.44
MetopC	-0.012	0.54	0.57	0.56	0.036	0.47
NOAA20	0.017	0.50	0.61	0.66	0.057	0.44
SNPP	0.016	0.51	0.64	0.67	0.052	0.47
Spring (March 1 – May 31, 2019)						
MetopB	0.019	0.68	0.59	0.64	0.045	0.46
MetopC	0.015	0.75	0.62	0.65	0.043	0.50
NOAA20	0.050	0.71	0.60	0.76	0.070	0.45
SNPP	0.045	0.72	0.62	0.74	0.063	0.47
Summer (June 1 – August 31, 2019)						
MetopB	0.036	0.77	0.57	0.77	0.033	0.52
MetopC	0.029	0.76	0.57	0.76	0.030	0.53
NOAA20	0.026	0.77	0.55	0.78	0.040	0.51
SNPP	0.028	0.80	0.55	0.78	0.040	0.52
Fall (September 1 – November 30, 2019)						
MetopB	0.006	0.52	0.61	0.64	0.032	0.47
MetopC	0.003	0.54	0.60	0.63	0.029	0.49
NOAA20	0.031	0.56	0.59	0.73	0.048	0.46
SNPP	0.025	0.56	0.60	0.71	0.043	0.47

Precipitation rate values are ≥ 0.
Precipitation rate threshold for calculating categorical scores is 0.6 mm/h.

TABLE V
SAME AS TABLE IV BUT VALIDATED BY MRMS

	Bias (mm/hr)	Stdv (mm/hr)	Corr	POD	FAR	HSS
Winter (December 1, 2018 – February 28, 2019)						
MetopB	-0.0018	0.48	0.56	0.52	0.040	0.42
MetopC	0.0002	0.44	0.60	0.57	0.034	0.46
NOAA20	0.023	0.41	0.62	0.64	0.052	0.43
SNPP	0.025	0.43	0.66	0.66	0.049	0.46
Spring (March 1 – May 31, 2019)						
MetopB	0.027	0.60	0.61	0.64	0.046	0.45
MetopC	0.025	0.66	0.63	0.67	0.043	0.48
NOAA20	0.066	0.63	0.60	0.77	0.074	0.43
SNPP	0.061	0.64	0.63	0.77	0.068	0.46
Summer (June 1 – August 31, 2019)						
MetopB	0.034	0.70	0.59	0.75	0.032	0.53
MetopC	0.027	0.68	0.59	0.74	0.029	0.54
NOAA20	0.038	0.71	0.58	0.78	0.043	0.51
SNPP	0.032	0.75	0.59	0.77	0.035	0.53
Fall (September 1 – November 30, 2019)						
MetopB	0.021	0.46	0.62	0.65	0.038	0.44
MetopC	0.015	0.47	0.63	0.63	0.032	0.47
NOAA20	0.046	0.51	0.60	0.73	0.054	0.42
SNPP	0.040	0.51	0.61	0.72	0.048	0.44

Precipitation rate values are ≥ 0.
Precipitation rate threshold for calculating categorical scores is 0.6 mm/h.

III. RESULTS AND DISCUSSION

Validation for MiRS retrieved precipitation rate from the four satellites against Stage-IV over CONUS are first illustrated by one single day (December 8, 2018) as shown in Fig. 1. The left column is the Stage-IV precipitation rate collocated with the corresponding MiRS precipitation rate for each satellite, which is shown in the middle column; top to bottom panels are MetopB, MetopC, NOAA20, and SNPP. Density scatterplots for each of the collocated Stage-IV and satellite pairs are shown in the third column, with gray points in the figure representing densities less than five.

On December 8, 2018, an intense winter storm system moved through the Gulf Coast toward the Southeast states bringing heavy precipitation in its path. Qualitatively, the MiRS precipitation rates retrieved from the four satellites (see Fig. 1, middle column) are very similar to their collocated Stage-IV ground observations (see Fig. 1, left column). Quantitatively, all satellites match the observed spatial distribution very well with spatial pattern correlations of 0.77 (MetopB), 0.72 (MetopC),

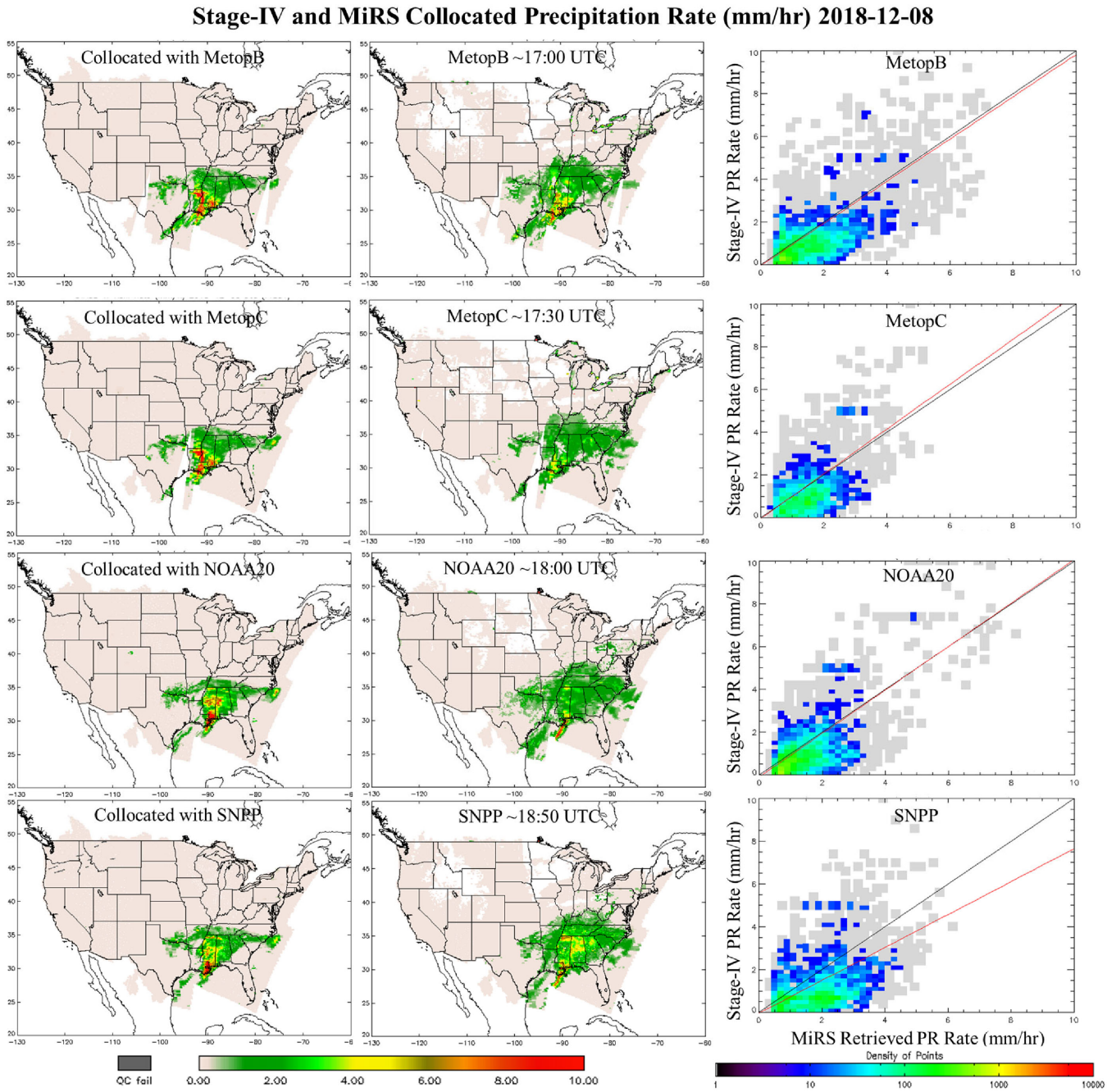

Fig. 1. Spatial precipitation rate (mm/h) distribution for collocated Stage-IV (left column) and MiRS retrievals (middle column) based on MetopB (first panel), MetopC (second panel), NOAA20 (third panel), and SNPP (last panel) for December 8, 2018. Density plots comparing MiRS and corresponding Stage-IV collocations are in the right column, gray points represent the density less than five points. Areas with no data in the MiRS retrieval were classified as snow covered.

0.75 (NOAA20), and 0.71 (SNPP). However MiRS shows a tendency to retrieve broader light precipitation coverage and somewhat less heavy precipitation. In order to have the four collocated Stage-IV precipitation rates as close as possible and in roughly the same precipitating area for easier comparison, MetopB (see Fig. 1 first panel) and MetopC (see Fig. 1 second panel) are from the descending pass, while NOAA20 (see Fig. 1 third panel) and SNPP (see Fig. 1 fourth panel) are from the ascending pass. The approximate times of the four satellite data are 17:00, 17:30, 18:00, and 18:50 UTC, respectively, based on the data in the vicinity of the storm system. The four MiRS retrievals are consistent with one another with discrepancies regarding detailed features. This may be expected given the different observation times and measurement geometry. The density plots (see Fig. 1, right column), show that for lighter precipitation (less than 3 mm/h), all the four retrievals are characterized by higher densities below 1:1 line, consistent with the observation above that the precipitation maps show a tendency for MiRS to have broader coverage of light precipitation than Stage-IV.

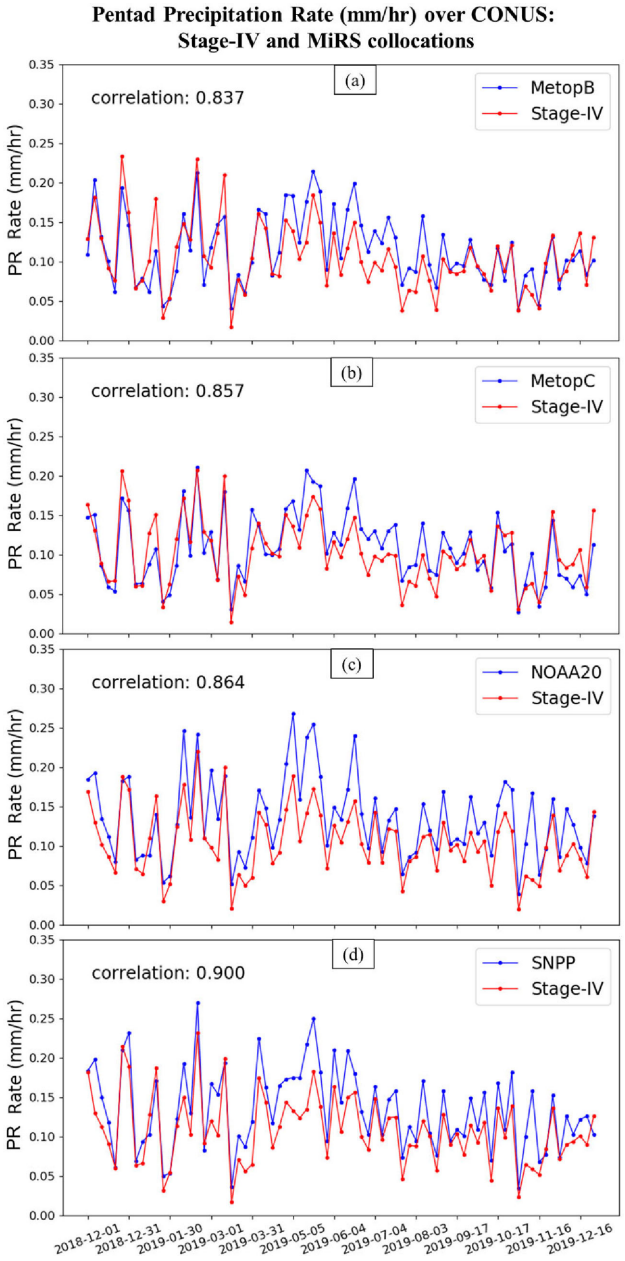

Fig. 2. Time series of pentad average precipitation rate (mm/h) over CONUS during December 1, 2018 to December 30, 2019 for MiRS (a) MetopB, (b) MetopC, (c) NOAA20, and (d) SNPP retrievals and the corresponding collocated Stage-IV.

Precipitation rate pentad time series during the period from December 1, 2018 to December 30, 2019 are shown in Fig. 2, with only land points over CONUS used in averaging (precipitation rates ≥ 0. mm/h). There are a total of 77 points plotted in Fig. 2, one for each 5-day period. NOAA20 and SNPP show a tendency to overestimate relative to Stage-IV values throughout the whole period, while MetopB and MetopC are higher mainly from April to July. This may be related to the retrieval tendency noted above for more extensive light precipitation coverage than Stage-IV. All four satellite retrievals vary with Stage-IV closely, and correlation coefficients with respect to Stage-IV are 0.83, 0.85, 0.86, and 0.90 for MetopB, MetopC, NOAA20, and SNPP, respectively (Table III). Table III also includes correlation coefficients validated against MRMS. The MetopB and MetopC values are slightly higher for MRMS than Stage-IV. In general, validation results against the two ground-based datasets are very similar.

Fig. 3 shows pentad time series for bias, standard deviation, correlation coefficient, probability of detection, false alarm rate, and HSS. The first three statistics are calculated for precipitation rate ≥ 0 mm/h; the other three categorical scores are calculated with a precipitation rate threshold of 0.6 mm/h. Biases [see Fig. 3(a)] for all the satellites vary between -0.05 and 0.1 mm/h. Biases are smaller (absolute value) and positive from April through September with SNPP and NOAA20 generally exhibiting larger values than either MetopB or MetopC. Standard deviations [see Fig. 3(b)] are between 0.2 and 1.0 mm/h with larger values typically found during the warm season, which is due to the generally higher precipiation rate ranges associated with convective weather systems. Correlation coefficients [see Fig. 3(c)] for all the satellites are also higher during warm season from March through October when they are greater than 0.5. Both the periods January to March and October to December in 2019 show larger variability and lower values than the warm season correlations. Probability of detection [see Fig. 3(d)] also shows higher and more stable values of greater than 0.7 during the warm season, and lower values and larger variability during the cold season. This variation feature is similar to that of the correlation coefficient [see Fig. 3(c)]. FARs [see Fig. 3(e)] are small from mid-June to mid-October (around 0.03), while other periods have relatively larger values. HSSs [see Fig. 3(f)] are typically larger than 0.5 in December 2018 and during March through October 2019, while they have lower values and vary largely for other days. In general, MiRS retrievals are more stable during warm season than cold season. Notwithstanding the larger biases noted for SNPP and NOAA20, retrievals from all four satellites have generally comparable performance, while at the same time exhibiting notable variability from one 5-day period to the next.

In order to reduce the impact of temporal variability seen in Fig. 3, Fig. 4 shows histograms for the same evaluation metrics for the four satellite retrievals but aggregated to monthly values for the period January 1 to December 31, 2019. Biases reflect those seen in Fig. 3, with the maximum value of 0.065 mm/h in May for NOAA20. Except for MetopB and MetopC in January, February, October, and December, all the values are positive, indicating MiRS overestimating the precipitation rate in comparison with the ground-based observations of Stage-IV, again consistent with the pentad time series. Standard deviations [see Fig. 4(b)] are higher in warm months (May–August) than cold months. As noted, this is somewhat expected due to the increased occurrence of heavier convective precipitation during the warm season, while cold season precipitation intensity is weaker and more uniform both spatially and temporally. This characteristic is also supported by the precipitation intensity frequency distributions shown in Fig. 5, which show significantly higher frequencies of precipitation rates greater than 6 mm/h during June–August. April has the highest correlation

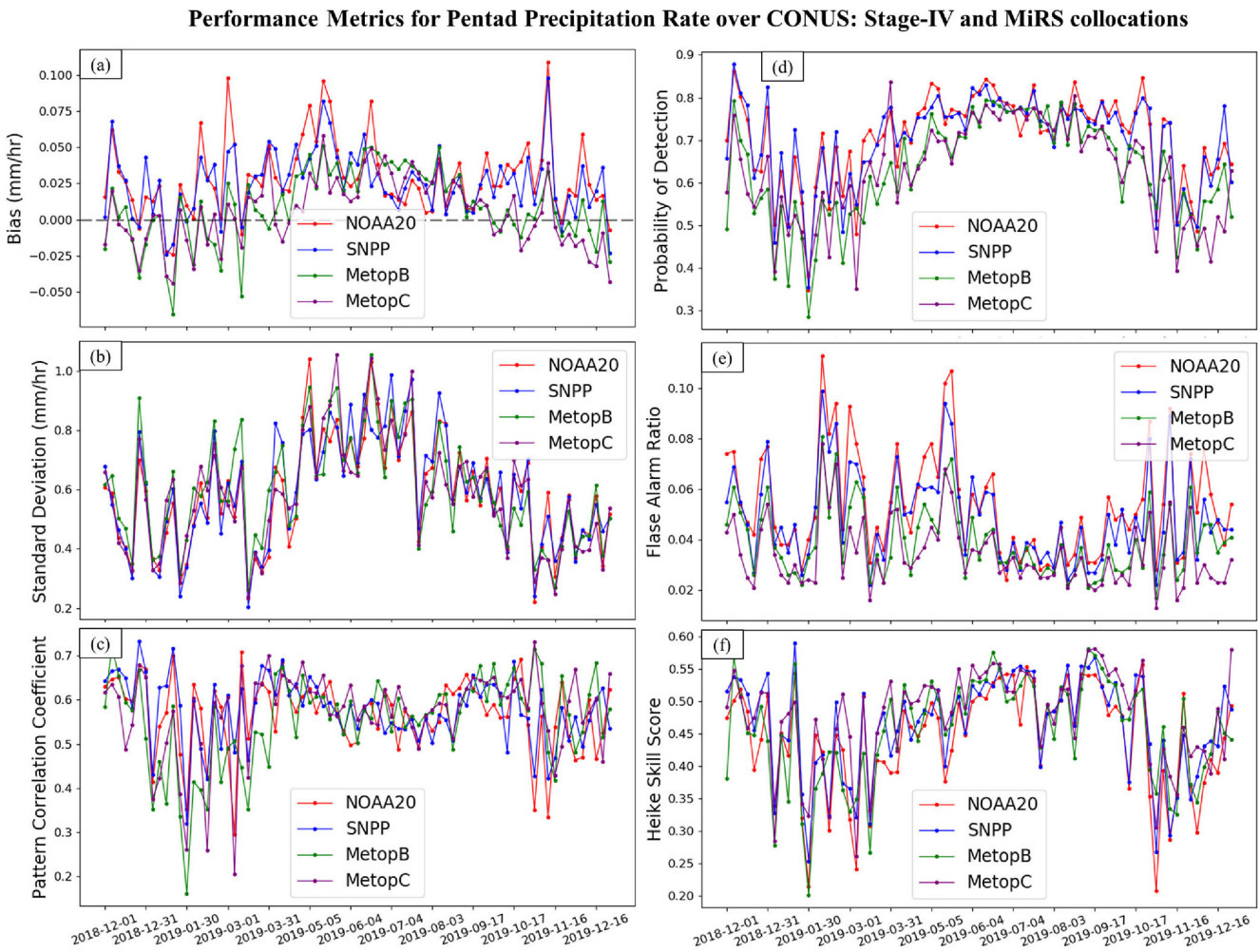

Fig. 3. Time series of evaluation statistics based on pentad precipitation rate over CONUS during December 1, 2018 to December 30, 2019 for MiRS NOAA-20, SNPP, MetopB, and MetopC retrievals against collocated Stage-IV for (a) bias (mm/h), (b) standard deviation (mm/h), (c) pattern correlation coefficient, (d) probability of detection, (e) FAR (probability of false detection), and (f) HSS. Precipitation rate values are ≥ 0, and the threshold for calculating categorical scores is 0.6 mm/h.

coefficients for all the satellites with values 0.63, 0.62, 0.63, and 0.68 for MetopB, MetopC, NOAA20, and SNPP, respectively. From April to October, all four satellites have similar correlations. While MetopB has substantially lower values than the other three satellites from January to March, MetopB and MetopC perform better than NOAA20 and SNPP in November and December. Regarding probability of detection [see Fig. 4(d)], all satellites have noticeably higher detection capability in warm months through April to October than other months. The scores are very close among the four satellites in July and August, while ATMS sensors (NOAA20 and SNPP) are higher than that of AMSUA-MHS (MetopB and MetopC) in all other months. ATMS retrievals have higher FARs [see Fig. 4(e)] than that of AMSUA-MHS during the whole year of 2019. Retrievals from NOAA20 and MetopC maintain the highest and lowest FAR consistently. All sensors have substantial smaller values in July–September. HSSs [see Fig. 4(f)] are also higher in warm months (June–October) than cold months, with November having the lowest score. The higher probability of detection and Heidke scores seen for all satellites during the warm season are also likely related to the increased importance of convective precipitation, which generally has a stronger microwave signal due to higher precipitation intensities and the presence of scattering by frozen hydrometeors, therefore allowing better detection and estimation.

Tables IV and V show the same performance metrics as the above but stratified by season and validation reference (Stage-IV and MRMS). Importantly, validation results are quite similar for Stage-IV and MRMS, despite the fact that the data are produced using different algorithms and have widely different spatial resolutions (4 km versus 0.01°). Biases are largest for NOAA20 during spring (0.05 mm/h) and the lowest for MetopC during fall (0.003 mm/h). During transition seasons of spring and fall, NOAA20 and SNPP have substantially higher biases than MetopB and MetopC, while having similar values during winter and summer. This feature is also seen in the bias pentad time series [see Fig. 3(a)]. Standard deviations are similar for the four satellite retrievals with higher values in warm seasons of spring and summer [consistent with Fig. 3(b)], which is characterized by higher precipitation intensity. In contrast to biases, spatial

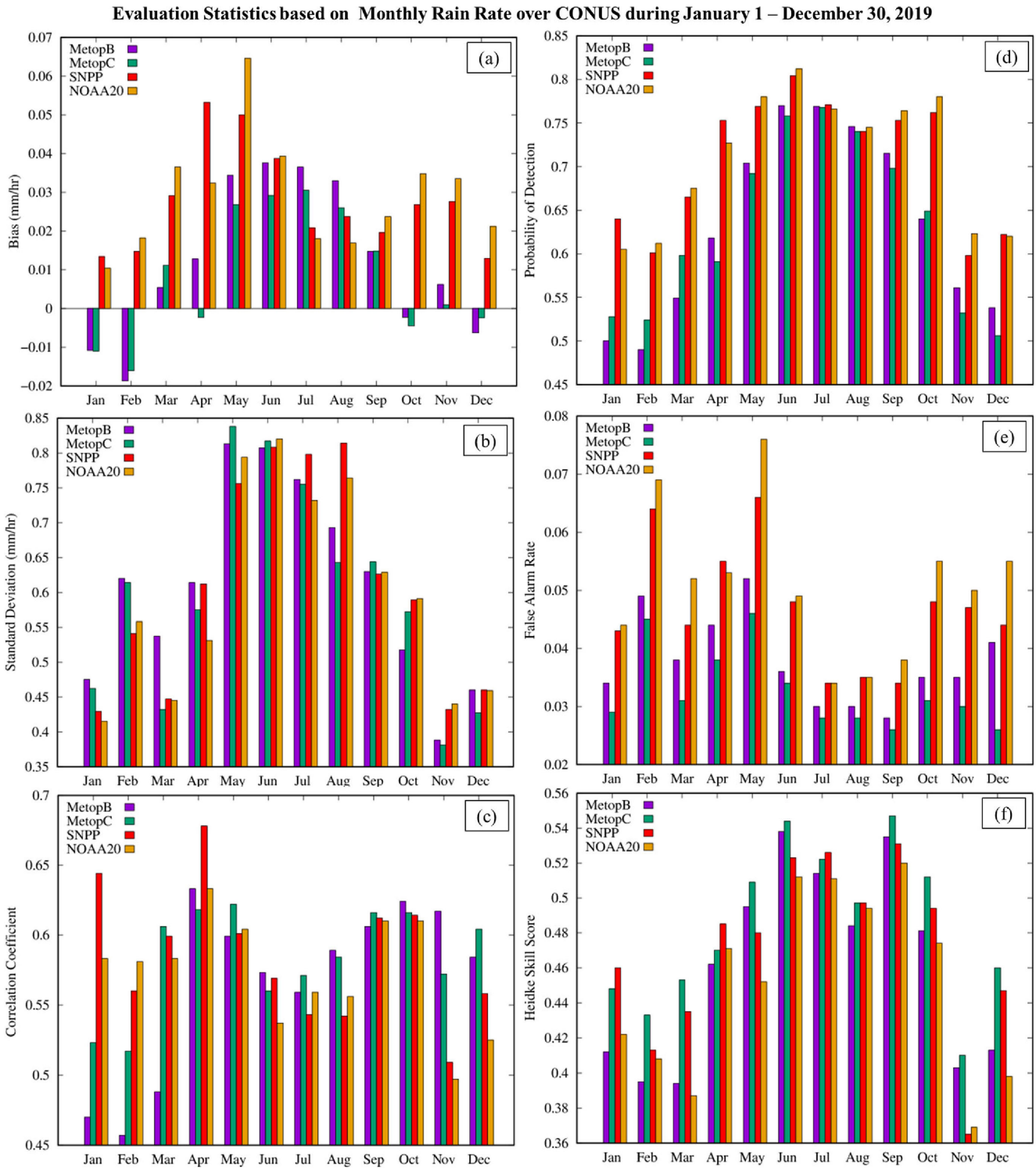

Fig. 4. Evaluation statistics based on monthly precipitation rate over CONUS during January 1, 2019 to December 30, 2019 for MiRS MetopB, MetopC, SNPP, and NOAA20 retrievals against collocated Stage-IV for (a) bias (mm/h), (b) standard deviation (mm/h), (c) correlation coefficient, (d) probability of detection, (e) false alarm rate, and (f) HSS. Precipitation rate values are ≥ 0, and the threshold for calculating categorical scores is 0.6 mm/h.

correlation coefficients are higher for NOAA20 and SNPP than MetopB and MetopC during spring and fall. This indicates that NOAA20 and SNPP captured precipitation spatial variability better than MetopB and MetopC while at the same time having larger biases during the two transition seasons. On the other hand, higher probability of detection and higher FAR are seen for NOAA20 and SNPP in comparison with MetopB and MetopC during spring, fall, and winter. However, HSSs only have small differences among the four satellites for all four seasons. All satellites show the highest HSS in summer.

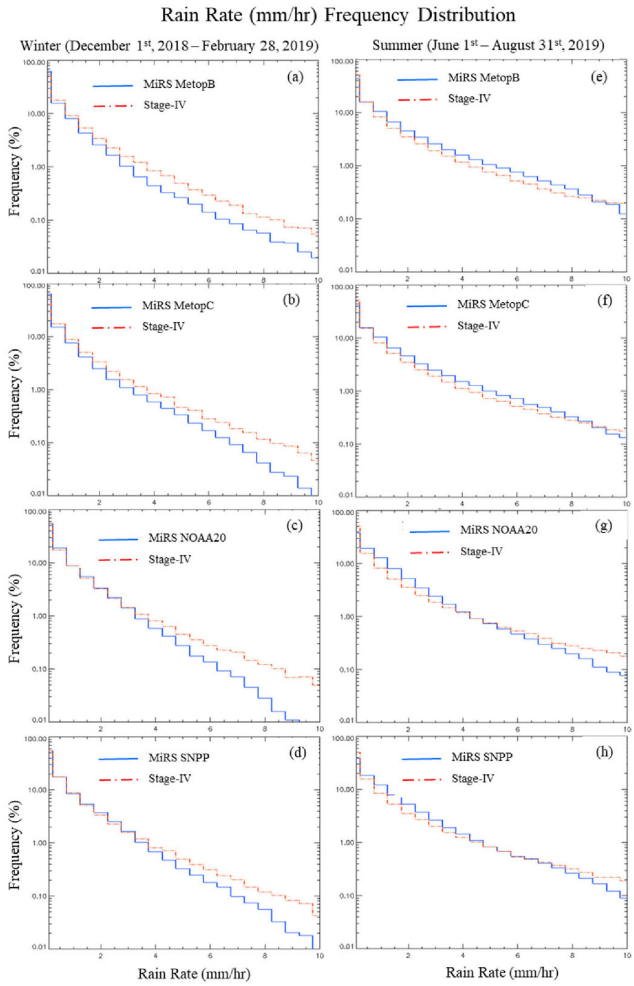

Fig. 5. Seasonal frequency distribution histograms for instantaneous precipitation rate (mm/h) for all four satellites relative to Stage-IV. Left: Winter (December– February) distributions. Right: Summer (June–August) distributions.

Analyses in previous sections are based on collocated MiRS and Stage-IV data which were then grouped on different time scales (daily, 5-day, monthly, and seasonal). To further characterize MiRS performance, we perform analyses based on precipitation intensity and regardless of the geolocation. Fig. 5 includes precipitation intensity frequency distribution histograms for winter (December–February, left column) and summer (June–August, right column) for NOAA20 (first panel), SNPP (second panel), MetopB (third panel), and MetopC (last panel). The vertical axis of frequency is in log scale, while the horizontal axis of precipitation rate is in linear scale and ranges from 0 to 10 mm/h, binned at 0.5 mm/h intervals. Each of the satellites shows substantially higher frequency of medium to heavy precipitation rates in summer than in winter. This seasonal difference is also seen in the Stage-IV ground-based observations (red line in Fig. 5). Compared with Stage-IV, generally, all the satellites underestimate precipitation frequency across the whole intensity range during winter with larger discrepancy for heavy precipitation. The ATMS (NOAA20 and SNPP) frequency for light precipitation (<3 mm/h) is very close to Stage-IV, indicating better skill in matching occurrence at these precipitation rates during winter. In summer (right column), MiRS and Stage-IV follow each other more closely. NOAA20 and SNPP produce slightly higher frequency than Stage-IV for light precipitation (<3 mm/h), very close for moderate precipitation (3–6 mm/h), and slightly lower frequency for heavy precipitation (>7 mm/h). MetopB and MetopC retrieval frequencies are very close to Stage-IV for very light precipitation (<1 mm/h) and heavy precipitation (>8 mm/h), while showing slight overestimation for the precipitation intensity for intermediate precipitation rates.

TABLE VI
PATTERN CORRELATION COEFFICIENTS FOR 2019 ANNUAL MEAN PRECIPITATION RATE AMONG SATELLITE RETRIEVALS AT 0.25° GRID

	NOAA20	SNPP	MetopB
SNPP	0.98		
MetopB	0.89	0.89	
MetopC	0.88	0.87	0.98

The annual global spatial distributions for MiRS precipitation rate from each of the four satellites averaged for the whole year of 2019 are shown in Fig. 6(a)–(d). Spatial pattern correlation coefficients among the four retrievals are listed in Table VI. Precipitation rates were retrieved at each sensor's native field-of-view (FOV) as indicated in Tables I and II and as described in Section II-B. To facilitate direct comparison and annual average calculation, precipitation rates in Fig. 6 were gridded to 0.25°, which is comparable to ATMS and AMUSA-MHS FOV size. The units were converted from gridded instantaneous millimeters per hour to millimeters per day by multiplying by 24. The belt associated with the intertropical convergence zone (ITCZ) is clearly depicted, with all the four satellites showing a narrow and concentrated zone at around 5°N latitude in the Western Hemisphere. In the Eastern Hemisphere, the heavy precipitation distribution features affected by the Asia summer monsoon are also identified. In the Northern Hemisphere, both Western Atlantic and Western Pacific precipitation distributions close to the American and Asian continents are depicted, with the maxima associated with the midlatitude storm tracks situated off the east coasts of both continents. Heavier precipitation over Eastern Pacific south of the equator is also noted. In the Southern Hemisphere, heavy precipitation associated with the Amazon rain forest region and over equatorial Africa is also retrieved. There are also some differences between the different satellite estimates. For example, the maxima of precipitation over the Amazon appear more intense in NOAA20 and SNPP. These satellites also depict larger precipitation areas with higher intensity over CONUS and China. This may be related to the temporal sampling differences of the NOAA versus Metop satellites relative to the diurnal cycle of precipitation. NOAA satellites have an equatorial crossing time of about 01:30 as compared to 09:30 for Metop, which may result in lower precipitation amounts for the Metop retrievals. There may also be a tendency for the AMTS-based retrievals to estimate slightly higher precipitation rates, as seen in some of the Stage-IV and MRMS

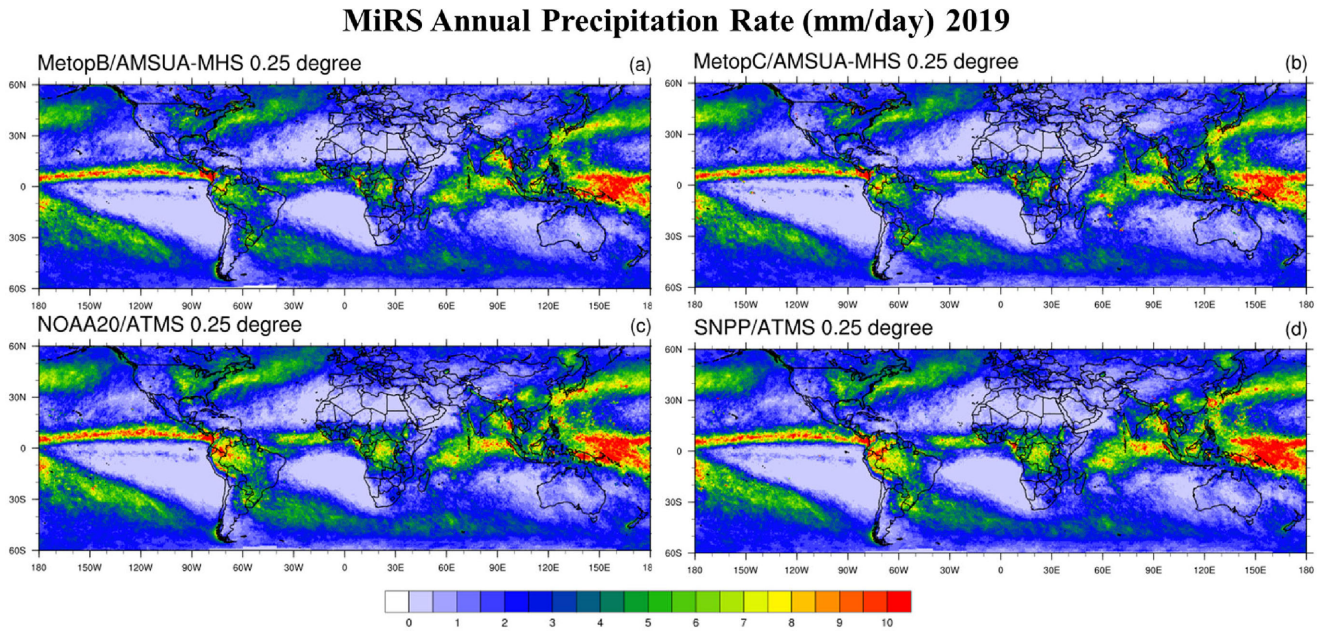

Fig. 6. Global annual precipitation rate (mm/day) distribution intercomparison for 2019 among MiRS for (a) MetopB/AMSUA-MHS, (b) MetopC/AMSUA-MHS, (c) NOAA20/ATMS, and (d) SNPP/ATMS. The precipitation rates are gridded to 0.25° resolution.

comparisons presented earlier. Nevertheless, the spatial intercorrelations between the different satellite averages are fairly high (see Table VI, >0.87), with the highest correlations between MetopB and MetopC, and between NOAA20 and SNPP (0.98). This is expected, as the MetopB/MetopC and SNPP/NOAA20 satellite pairs are operating with very similar local crossing times.

Fig. 7(a) shows the composite (average of the four satellite retrievals) of the four satellites and regridded to 1.0° to facilitate comparison with the official estimate of the Global Precipitation Climatology Project (GPCP) [34]. Fig. 7(b) is GPCP 2019 annual precipitation calculated from version 2.3 daily records. Differences between the MiRS four-satellite composite and GPCP are shown in Fig. 7(c). The MiRS composite precipitation shows a very similar global distribution with GPCP with a pattern correlation coefficient of 0.96. Over land precipitation shows larger differences than those over ocean [see Fig. 7(c)]. The estimates over central CONUS and north central China also show noticeably higher precipitation rates in the MiRS composite than GPCP. Conversely, areas of the Amazon basin, southeast Asia, and along the Pacific Ocean ITCZ show lower MiRS estimates than GPCP. Given the increased sampling of the diurnal precipitation cycle, it is expected that the four-satellite composite would be more accurate than any of the individual estimates, although a more detailed quantitative assessment is not presented here. The GPCP analyses incorporate a broader range of both space- and ground-based observations and are expected to be more accurate. Future efforts will focus on quantifying the differences between the MiRS global estimates from the different satellites, as well as with those from independent satellite precipitation products, for example, the Integrated Multi-satellitE Retrievals for GPM (IMERG) product [35].

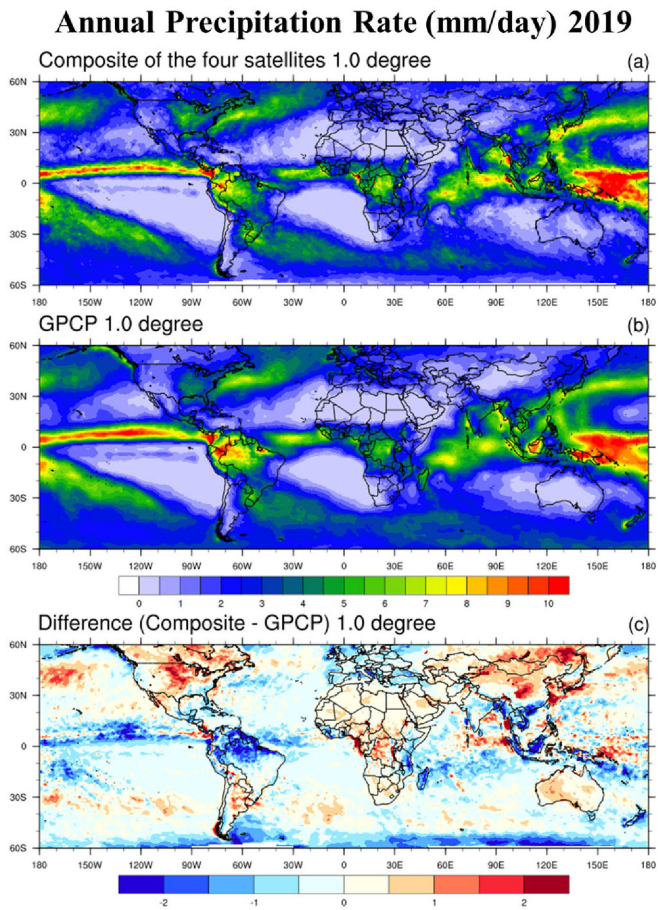

Fig. 7. Global annual precipitation rate (mm/day) distribution for 2019. (a) Composite of four satellite retrievals. (b) GPCP. (c) Difference between composite and GPCP. The precipitation rates are gridded to 1.0° resolution.

IV. Conclusion

MiRS uses the same 1-DVAR approach within a common framework to retrieve a comprehensive suite of atmospheric and surface parameters from passive microwave measurements for all supported satellites. This characteristic provides an opportunity to utilize MiRS precipitation products from the suite of polar-orbiting satellites currently processed by MiRS (i.e., NOAA18, NOAA19, SNPP, NOAA20, MetopB, MetopC, GPM, and DMSP F17 and F18) for a more comprehensive monitoring of precipitation events around the globe.

In order to assess the performance and consistency of the algorithm, in this article, we performed a validation intercomparison for the period from December 1, 2018 to December 31, 2019 of MiRS precipitation retrievals from four operational polar satellites: NOAA20/ATMS, SNPP/ATMS, MetopB/AMSUA-MHS, and MetopC/AMSUA-MHS. Two reference datasets were used to evaluate the performance—the operational Stage-IV and MRMS rain gauge and radar composite analyses over CONUS. Analysis was performed by first collocating the satellite instantaneous estimates with the accumulated hourly Stage-IV values, while accounting for changes in the satellite FOV size with scan angle. Comparisons were made at hourly, pentad, and monthly time scales over CONUS. Global maps of annual average precipitation rates were also constructed. The primary results of the analysis were the following.

1) Precipitation rate pentad time series showed relatively good agreement with Stage-IV observations, with similar seasonal variations between MiRS and Stage-IV estimates.
2) Time series of statistical and categorical scores (correlation, probability of detection, and Heidke score) showed more stable and higher performance during the warm season, consistent with previous studies. Pentad time series showed relatively large temporal variability from one time period to another, especially during winter, fall, and spring seasons.
3) Precipitation estimates from SNPP and NOAA20 appeared to have a somewhat larger bias with respect to Stage-IV than MetopB and MetopC, with the exception of July and August 2019.
4) Frequency distributions of precipitation intensity also showed better agreement between MiRS and Stage-IV for higher precipitation rates ($>$6 mm/h) in the warm season, highlighting the difficulty of estimating over land precipitation rates associated with stratiform precipitation systems that typically occur during the cold season.
5) All satellites depicted the annual mean precipitation rate geophysical distribution over the globe with good interconsistency, but also with some differences that may be related to individual temporal sampling characteristics of each satellite. Comparison with the GPCP annual mean precipitation rate for the same time period showed good agreement on the large-scale spatial patterns, but regional differences were also noted.
6) An identical set of validation comparisons were performed using the MRMS operational precipitation product. Details were not shown, but summary validation statistics and scores stratified by season show that performance metrics when using MRMS as a reference are largely similar to those based on using Stage-IV.

The results presented here indicate that the MiRS precipitation estimates from multiple polar-orbiting satellites may be effective in filling some of the temporal and spatial gaps presented by a single satellite. This is due in part to the interconsistency of the estimates from each satellite, and stems from the use of a common algorithm across all satellites. Future studies will be directed at further quantifying the performance and performance differences of precipitation products from NOAA18, NOAA19, GPM, and DMSP (F17, F18), in addition to the satellites analyzed in this study. Comparison with other independent precipitation products will also be investigated, particularly for estimates over ocean regions.

Acknowledgment

The manuscript contents are solely the opinions of the authors and do not constitute a statement of policy, decision, or position on behalf of NOAA or the U.S. Government.

References

[1] P. A. Arkin and B. N. Meisner, "The relationship between large-scale convective rainfall and cold cloud over the Western Hemisphere during 1982-84," *Monthly Weather Rev.*, vol. 115, no. 1, pp. 51–74, 1987.

[2] T. T. Wilheit, A. T. C. Chang, and L. S. Chiu, "Retrieval of monthly rainfall indices from microwave radiometric measurement using probability distribution functions," *J. Atmos. Ocean. Technol.*, vol. 8, pp. 118–136, 1991.

[3] W. Berg and R. Chas, "Determination of mean rainfall from the special sensor microwave/imager (SSM/I) using a mixed lognormal distribution," *J. Atmos. Ocean. Technol.*, vol. 9, pp. 129–141, 1992.

[4] N. C. Grody, "Classification of snow cover and precipitation using the special sensor microwave/imager (SSM/I)," *J. Geophys. Res.*, vol. 96, pp. 7423–7435, 1991.

[5] R. R. Ferraro and G. F. Marks, "The development of SSM/I rain-rate retrieval algorithms using ground-based radar measurements," *J. Atmos. Ocean. Technol.*, vol. 12, pp. 755–770, 1995.

[6] A. E. Mugnai, A. Smith, and G. J. Tripoli, "Foundations for statistical–physical precipitation retrieval from passive microwave satellite measurements. Part II: Emission-source and generalized weighting-function properties of a time-dependent cloud-radiation model," *J. Appl. Meteorol.*, vol. 32, pp. 17–39, 1993.

[7] C. Kummerow and L. Giglio, "A passive microwave technique for estimating rainfall and vertical structure information from space. Part I: Algorithm description," *J. Appl. Meteorol.*, vol. 33, pp. 3–18, 1994.

[8] E. A. Smith, X. Xiang, A. Mugnai, and G. Tripoli, "Design of an inversion-based precipitation profile retrieval algorithm using an explicit cloud model for initial guess microphysics," *Meteorol. Atmos. Phys.*, vol. 54, pp. 53–78, 1994.

[9] G. W. Petty, "Physical retrievals of over-ocean rain rate from multichannel microwave imagery. Part I: Theoretical characteristics of normalized polarization and scattering indices," *Meteorol. Atmos. Phys.*, vol. 54, pp. 79–99, 1994.

[10] T. T. Wilheit *et al.*, "Algorithms for the retrieval of rainfall from passive microwave measurements," *Remote Sens. Rev.*, vol. 11, no. 1/4, pp. 163–194, Oct. 2004.

[11] G. W. Petty, "Physical retrievals of over-ocean rain rate from multichannel microwave imagery. Part II: Algorithm implementation," *Meteorol. Atmos. Phys.*, vol. 54, no. 1/4, pp. 101–121, Mar. 1994.

[12] A. T. C. Chang, L. S. Chiu, C. Kummerow, and J. Meng, "First results of the TRMM microwave imager (TMI) monthly oceanic rain rate: Comparison with SSM/I," *Geophys. Res. Lett.*, vol. 26, pp. 2379–2382, 1999.

[13] C. D. Kummerow *et al.*, "The evolution of the Goddard profiling algorithm (GPROF) for rainfall estimation from passive microwave sensors," *J. Appl. Meteorol.*, vol. 40, no. 11, pp. 1801–1820, Nov. 2001.

[14] C. D. Kummerow *et al.*, "The evolution of the Goddard profiling algorithm to a fully parametric scheme," *J. Atmos. Ocean. Technol.*, vol. 32, pp. 2265–2280, Dec. 2015.

[15] R. R. Ferraro *et al.*, "NOAA operational hydrological products derived from the advanced microwave sounding unit," *IEEE Trans. Geosci. Remote Sens.*, vol. 43, no. 5, pp. 1036–1049, May 2005.

[16] C. Surussavadee and D. H. Staelin, "Satellite retrievals of Arctic and Equatorial rain and snowfall rates using millimeter wavelengths," *IEEE Trans. Geosci. Remote Sens.*, vol. 47, no. 11, pp. 3697–3707, Nov. 2009.

[17] S.-A. Boukabara, F. Weng, and Q. Liu, "Passive microwave remote sensing of extreme weather events using NOAA-18 AMSUA and MHS," *IEEE Trans. Geosci. Remote Sens.*, vol. 45, no. 7, pp. 2228–2246, Jul. 2007.

[18] S.-A. Boukabara *et al.*, "MiRS: An all-weather 1DVAR satellite data assimilation and retrieval system," *IEEE Trans. Geosci. Remote Sens.* vol. 49, no. 9, pp. 3249–3272, Sep. 2011.

[19] F. Iturbide-Sanchez *et al.*, "Assessment of a variational inversion system for rainfall rate over land and water surfaces," *IEEE Trans. Geosci. Remote Sens.*, vol. 49, no. 9, pp. 3311–3333, Sep. 2011.

[20] S. Liu, C. Grassotti, J. Chen, and Q. Liu, "GPM products from the mircrowave integrated retrieval system (MiRS)," *IEEE J. Sel. Topics Appl. Earth Observ. Remote Sens.*, vol. 10, no. 6, 2565–2574, Jun. 2017.

[21] R. Joyce, J. E. Janowiak, P. A. Arkin, and P. Xie, "CMORPH: A method that produces global precipitation estimates from passive microwave and infrared data at high spatial and temporal resolution," *J. Hydrometeorol.*, vol. 5, pp. 487–503, 2004.

[22] P. Xie *et al.*, "Reprocessed bias-corrected CMORPH global high-resolution precipitation esteimates from 1998," *J. Hydrometeorol.*, vol. 18, pp. 1617–1641, 2017.

[23] C. D. Rodgers, *Inverse Methods for Atmospheric Sounding: Theory and Practice*. Singapore: World Scientific, 2000.

[24] Q. Liu and F. Weng, "One-dimensional retrieval algorithm of temperature, water vapor, and cloud water profiles from advanced microwave sounding unit (AMSU)," *IEEE Trans. Geosci. Remote Sens.*, vol. 43, no. 5, 1087–1095, May 2005.

[25] F. Weng *et al.*, "JCSDA community radiative transfer model (CRTM)," in *Proc. 14th TOVS Conf.*, Beijing, China, 2005, pp. 217–222.

[26] Y. Han *et al.*, "Community radiative transfer model (CRTM)," Dept. Commerce, Washington, DC, USA, NOAA Tech. Rep. 122, version 1, 2006.

[27] Y. Chen, F. Weng, Y. Han, and Q. Liu, "Validation of the community radiative transfer model (CRTM) by using CloudSat data," *J. Geophys. Res.*, vol. 113, no. D8, pp. 2156–2202, 2008.

[28] S. Ding *et al.*, "Validation of the community radiative transfer model," *J. Quant. Spectrosc. Radiat. Transfer*, vol. 112, no. 6, pp. 1050–1064, 2011.

[29] S. Liu, C. Grassotti, and Q. Liu, "2018: NOAA microwave integrated retrieval system (MiRS) cloud liquid water retrieval and assessment," in *Proc. IEEE 15th Spec. Meeting Microw. Radiometry Remote Sens. Environ.*, 2018, pp. 14–19.

[30] S. Kida, S. Shiqe, T. Manabe, T. S. L'Ecuyer, and G. Liu, "Validation of rain/non-rain threshold value of cloud liquid water for microwave precipitation retrieval algorithm using CloudSat precipitation product," *Proc. SPIE*, vol. 7152, pp. 715209-1–715209-8, 2008.

[31] Y. Lin and K. E. Mitchell, "The NCEP Stage II/IV hourly precipitation analyses: Development and applications," in *Proc. 19th Conf. Hydrol. Amer. Meteorol. Soc. 1.2*, San Diego, CA, USA, 2005. [Online]. Available: http://ams.confex.com/ams/Annual2005/techprogram/paper_83847.htm

[32] H. E. Brooks and C. A. Doswell, III, "A comparison of measures-oriented and distributions-oriented approaches to forecast verification," *Weather Forecasting*, vol. 11, pp. 288–303, 1996.

[33] J. Zhang *et al.*, "Multi-radar multi-sensor (MRMS) quantitative precipitation estimation: Initial operating capabilities," *Bull. Amer. Meteorol. Soc.*, vol. 97, no. 4, pp. 621–638, 2016.

[34] G. J. Huffman, R. F. Adler, D. T. Bolvin, and G. Gu, "Improving the global precipitation record: GPCP version 2.1," *Geophys. Res. Lett.*, vol. 36, 2009, Art. no. L17808.

[35] Z. Liu, "Comparison of integrated multisatellite retrievals for GPM (IMERG) and TRMM multisatellite precipitation analysis (TMPA) monthly precipitation products: Initial results," *J. Hydrometeorol.*, vol. 17, pp. 777–790, 2016.

Shuyan Liu received the B.S. and M.S. degrees in atmospheric physics and environment from the Nanjing Institute of Meteorology, Nanjing, China, in 2000 and 2003, respectively, and the Ph.D. degree in meteorology from the Nanjing University of Information Science and Technology, Nanjing, China, in 2006.

From 2007 to 2011, she was a Climate Model Developer with Illinois State Water Survey, University of Illinois at Urbana-Champaign, Champaign, IL, USA. From 2011 to 2015, she was with Earth System Science Interdisciplinary Center, University of Maryland, College Park, MD, USA. Since 2015, she has been with the Cooperative Institute for Research in the Atmosphere (CIRA), Colorado State University, Fort Collins, CO, USA, and the NOAA Center for Satellite Applications and Research, National Environmental Satellite, Data, and Information Service, College Park, MD, USA.

Christopher Grassotti received the B.S. degree in earth and space science from the State University of New York at Stony Brook, Stony Brook, NY, USA, in 1982, the M.S. degree in meteorology from the University of Wisconsin-Madison, Madison, WI, USA, in 1986, and the M.S. degree in viticulture and enology from AgroMontpellier, Montpellier, France, in 2007.

From 1986 to 1991 and again from 1993 to 2005, he was a Research Associate and Senior Research Associate with Atmospheric and Environmental Research, Inc., Lexington, MA, USA. From 1991 to 1993, he was with the Atmospheric Environmental Service, Environment Canada, Dorval, QC, Canada. Since 2008, he has been with the National Oceanic and Atmospheric Administration, NOAA Center for Satellite Applications and Research, National Environmental Satellite, Data, and Information Service, College Park, MD, USA.

Quanhua Liu received the B.S. degree in physics from the Nanjing University of Information Science and Technology (formerly Nanjing Institute of Meteorology), Nanjing, China, in 1982, the master's degree in physics from the Chinese Academy of Science, Beijing, China, in 1984, and the Ph.D. degree in meteorology and remote sensing from the University of Kiel, Kiel, Germany, in 1991.

He is currently a Physical Scientist with the National Oceanic and Atmospheric Administration, National Environmental Satellite, Data, and Information Service, College Park, MD, USA, and is leading the soundings team at NOAA Center for Satellite Applications and Research (NOAA/STAR), College Park, MD, USA. The sounding system utilized satellite-based microwave observations and infrared hyperspectral measurements to acquire vertical profiles of atmospheric temperature, water vapor, ozone, CO, CH_4, CO_2, and others chemical species. He studied the infrared hyperspectral sensor and the community radiative transfer model (CRTM). The CRTM has been operationally supporting satellite radiance assimilation for weather forecasting. The CRTM also supports JPSS/NPP and GOES-R missions for instrument calibration, validation, long-term trend monitoring, and satellite retrieved products.

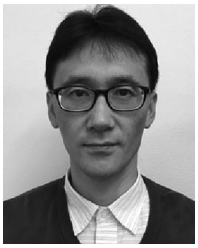

Yong-Keun Lee received the B.S. and the M.S. degrees from Seoul National University, Seoul, South Korea, in 1994 and 1996, respectively, and the Ph.D. degree from Texas A&M University, College Station, TX, USA, in 2006, all in atmospheric science.

From 2006 to 2018, he was with the Space Science and Engineering Center, University of Wisconsin, WI, USA. Since 2018, he has been with the Earth System Science Interdisciplinary Center, University of Maryland, College Park, MD USA, and the National Oceanic and Atmospheric Administration, NOAA Center for Satellite Applications and Research, National Environmental Satellites, Data, and Information Service, College Park, MD, USA.

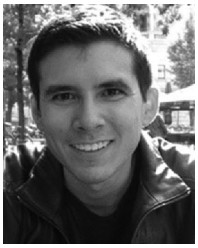

Ryan Honeyager received the B.S. degree in physics from the University of Florida, Gainesville, FL, USA, in 2010, and the M.S. and Ph.D. degrees in meteorology from Florida State University, Tallahassee, FL, USA, in 2013 and 2017, respectively.

He is a Scientist with the National Oceanic and Atmospheric Administration (NOAA) Center for Weather and Climate Prediction, College Park, MD, USA. Since 2018, he has been working on both the Microwave Integrated Retrieval System (MiRS) and the Joint Effort for Data Assimilation Integration (JEDI) Projects and is currently the Joint Center for Satellite Data Assimilation's liaison to the NOAA Environmental Modeling Center.

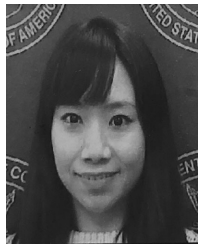

Yan Zhou received the B.S. degree from Zhejiang University, Hangzhou, China, in 2006, the M.S. degree from the University of Georgia, Athens, GA, USA, in 2008, and the Ph.D. degree from the University of Maryland, College Park, MD, USA, in 2014, all in the major of atmospheric science.

From 2015 to 2018, she worked on the CICS-MD Observing System Simulation Experiment (OSSE) Project with the Earth System Science Interdisciplinary Center (ESSIC), University of Maryland. Since 2019, she has been with the ESSIC, in cooperation with NOAA Center for Satellite Applications and Research (NOAA/STAR), College Park, MD, USA, working on the Microwave Integrated Retrieval System (MiRS) Project.

Ming Fang received the B.S. degree in atmospheric physics from the Nanjing University of Information Science and Technology (formerly Nanjing Institute of Meteorology), Nanjing, China, in 1983, and the master's and Ph.D. degrees in meteorology from the University of Oklahoma, Norman, OK, USA, in 2005 and 2008, respectively.

From 2006 to 2009, he was a Research Associate with the Cooperative Institution for Mesoscale Meteorological Studies, University of Oklahoma. From 2009 to 2017, he was an Associate Research Scientist with the Rosenstiel School of Marine and Atmospheric Science, University of Miami, Coral Gables, FL, USA. From 2017 to 2019, he was a Senior Scientist with Aviation Meteorology Division, I.M. Systems Group Inc., Rockville, MD, USA. Since 2019, he has been with I.M. Systems Group Inc. and the National Oceanic and Atmospheric Administration, NOAA Center for Satellite Applications and Research, National Environmental Satellite, Data, and Information Service, College Park, MD, USA.